RSC Advances

PAPER

View Article Online
View Journal | View Issue

Cite this: *RSC Adv.*, 2022, **12**, 22367

Synthesis of a UiO-66/g-C_3N_4 composite using terephthalic acid obtained from waste plastic for the photocatalytic degradation of the chemical warfare agent simulant, methyl paraoxon†

Dung Van Le,[ab] Manh B. Nguyen,*[c] Phuong T. Dang,[c] Taeyoon Lee*[d] and Trinh Duy Nguyen *[ae]

In our study, Zr-based UiO-66 (Zr) was synthesized using terephthalic acid obtained from waste plastic. Thereafter, UiO-66/g-C_3N_4 composites were prepared by the solvothermal method, and their photocatalytic activity in the photodegradation of the chemical warfare agent simulant, dimethyl 4-nitrophenyl phosphate (DMNP), was evaluated. The as-synthesized UiO-66/g-C_3N_4 exhibited a high surface area (1440 m^2 g^{-1}) and a high capillary volume (1.49 cm^3 g^{-1}). The UiO-66/g-C_3N_4 samples absorbed a visible light band with bandgap energies of 2.13–2.88 eV. The as-synthesized UiO-66/g-C_3N_4 composites exhibited highly efficient degradation of DMNP with a short half-life ($t_{1/2}$ of 2.17 min) at pH 7 under visible light irradiation. The trapping experiments confirmed that the h^+ and $^{\bullet}O_2^-$ radicals played an important role in the photocatalytic degradation of DMNP. The UiO-66/g-C_3N_4 catalyst simultaneously performed two processes: the hydrolysis and photocatalytic oxidation of DMNP in water. During irradiation, a p–n heterojunction between UiO-66 and g-C_3N_4 restricted the recombination of photogenerated electrons and holes, resulting in the enhancement in the degradation rate of DMNP.

Received 5th June 2022
Accepted 3rd August 2022

DOI: 10.1039/d2ra03483b

rsc.li/rsc-advances

1 Introduction

Organophosphate ester compounds have been used to synthesize a variety of organic chemicals, such as drugs, pesticides, herbicides, fungicides, flame retardants, surfactants, and dangerous neurotoxins.[1,2] The highly dangerous neurotoxins known as chemical warfare agents (CWAs) can affect the respiratory system, cause severe damage, and destroy the central nervous system, leading to death.[2] Therefore, the rapid decomposition and conversion of CWAs into environmentally friendly and non-toxic products have been considered an urgent issue.[3,4] Several disinfectants have been applied to treat CWAs, such as bleach or salt, porous organic polymers, metal oxides, potassium persulphate, ozone, sodium hypochlorite, and hydrogen peroxide.[5–7] However, the above disinfectants have limitations, such as high corrosiveness, instability, environmental impact, and long processing duration.[8]

The degradation of CWAs over photocatalysts has recently been receiving considerable attention because these materials can degrade CWAs into non-toxic products. For example, Zr-based metal–organic frameworks (MOFs), including UiO-66 and NH_2-UiO-66, have recently been used as effective photocatalysts to degrade CWAs and its simulant, dimethyl 4-nitrophenyl phosphate (DMNP).[3,8] However, the DMNP treatment process is performed in alkaline media (pH = 10) using *N*-ethylmorpholine buffer solution; thus, it is difficult to apply in the industry.[6] Furthermore, Zr-based MOFs become less stable at pH greater than 9.5, in which the surface area of the Zr-based MOFs significantly decreases, and a large amount of terephthalic acid is released into the solution.[9] Similarly, Song *et al.*[8] reported that the treatment efficiency of DMNP over graphene@UiO-66-NH_2 composite is strongly influenced by the pH and concentration of the *N*-ethylmorpholine buffer solution. Further, they have shown that the graphene@UiO-66-NH_2 composite exhibits a low efficiency for DMNP removal (approximately 49%) in water media without using the *N*-ethylmorpholine buffer solution. Additionally, organophosphates

[a]*Graduate University of Science and Technology, Vietnam Academy of Science and Technology, 18 Hoang Quoc Viet Street, Cau Giay, Ha Noi, Vietnam*
[b]*Center for Technology Environmental Treatment, 282 Lac Long Quan Street, Tay Ho, Ha Noi, Vietnam*
[c]*Institute of Chemistry, Vietnam Academy of Science and Technology, 18 Hoang Quoc Viet Street, Cau Giay, Ha Noi, Vietnam. E-mail: nguyenbamanh@ich.vast.vn*
[d]*Department of Environmental Engineering, College of Environmental and Marine, Pukyong National University, 45 Yongso-ro, Nam-gu, Busan, 48513, Republic of Korea. E-mail: badger74w@pknu.ac.kr*
[e]*Institute of Applied Technology and Sustainable Development, Nguyen Tat Thanh University, Ho Chi Minh City, Vietnam. E-mail: ndtrinh@ntt.edu.vn*

† Electronic supplementary information (ESI) available: HPLC spectrum of H_2BDC, schematic synthesis of UiO-66/g-C_3N_4, XRD analysis, EDS spectra, SEM images, UV-vis spectra of DMNP, images of DMNP solution, LC-mass spectra of DMNP, photo-stability test, element composition, and a comparison of photocatalytic activity of photocatalysts. See https://doi.org/10.1039/d2ra03483b

can be slowly hydrolyzed in water to form other toxic substances, such as methyl 4-nitrophenyl phosphate (M4NP).[2] To enhance the removal efficiency of the CWAs in an aqueous medium, MOF (Zr) catalysts modified with amines, graphene, and metal alkoxides groups have been reported.[10–12] Song *et al.*[8] reported that graphene@UiO-66-NH_2 significantly increased the degradation rate of DMNP, and the half-life decreased from 3.4 to 1.6 min using sunlight irradiation.

Recently, a metal-free semiconductor, g-C_3N_4, has been widely studied and applied as a photocatalyst for energy production, electrocatalysis, and electrochemiluminescence.[13–19] The g-C_3N_4 semiconductor possesses many advantages, such as low production cost, simple fabrication, strong oxidizing properties, high thermal stability, high chemical stability, and excellent optical and thermal properties.[20–22] However, g-C_3N_4 has a low surface area (10–30 $m^2\ g^{-1}$), easily formed electron–hole pairs, fast charge recombination, nature chemical inertness, bulky structure, and bulky size.[23–28] Therefore, modifying g-C_3N_4 with carbon-based materials[29] or MOFs[30] or dissecting g-C_3N_4 into monolayer nanosheets produces thin layers that improve the surface area and enhance the diffusion rate of reactants/products.[31] MOFs/g-C_3N_4 heterojunction catalysts have been studied because they can effectively block the fast recombination ability of electron (e^-) and hole (h^+) pairs and absorb high visible light, thereby increasing the efficiency of the photocatalyst. Furthermore, the π–π conjugate structure between g-C_3N_4 and UiO-66 can induce a high charge-separation rate.[32]

In our study, we use terephthalic acid produced from waste plastics to synthesize low-cost UiO-66 catalysts. The conversion of plastic waste to valuable products is considered an economically and environmentally friendly solution. Afterward, the UiO-66/g-C_3N_4 heterojunction catalysts are synthesized by the solvothermal method. The UiO-66/g-C_3N_4 catalysts are applied for the hydrolysis and photocatalytic oxidation of the CWA simulant, DMNP, in an aqueous environment. The UiO-66/g-C_3N_4 catalysts possess advantages, such as (i) high surface area, (ii) enhanced visible light absorption, and (iii) low recombination of photogenerated electrons and holes. Therefore, the photocatalytic oxidation of the DMNP is improved.

2 Materials and methods

2.1 Material

Polyethylene terephthalate (PET) water bottles were used as a source of plastic waste to prepare terephthalic acid (H_2BDC). The chemical reagents used in this study, including sulphuric acid (H_2SO_4, 98%), hydroxyl sodium (NaOH, 98%), dimethylformamide (DMF, 98%), ethylene glycol (EG), *N*-ethylmorpholine, zirconyl chloride octahydrate ($ZrOCl_2 \cdot 8H_2O$, 98%), cetyltrimethylammonium bromide (CTABr, 98%) and dimethyl 4-nitrophenyl phosphate (DMNP, 99%), were supplied by Sigma-Aldrich.

2.2 Synthesis of H_2BDC from waste plastic

PET water bottles purchased from recycling facilities were cleaned, dried, and cut into 4 × 4 mm pieces. Next, a mixture of the waste PET pieces (24 g), NaOH (44 g), and EG (110 mL) was added to a 500 mL three-necked flask equipped with a condenser. The mixture was vigorously stirred at 300 rpm and heated at 190 °C for 3 h. Afterward, the mixture was cooled to 80 °C, and 200 mL of distilled water was added; the mixture was stirred until completely dissolved. The pH of the mixture was adjusted to 3 using 2 M H_2SO_4 to obtain a white slurry. Finally, the obtained H_2BDC was filtered and washed four times with distilled water and dried overnight at 60 °C. HPLC spectrum of H_2BDC product (Fig. S1†) shows a large peak at retention time at 3.171 minutes and a small peak at a retention time at 3.976 minutes, indicating that the main component H_2BDC is about 99% after the refining process. The H_2BDC production obtained about 73.4% yields.

2.3 Synthesis of the UiO-66 and UiO-66/g-C_3N_4 composites

The g-C_3N_4 was synthesized by calcination, as reported in the literature.[31,33] Briefly, 10 g of urea and 10 g of NH_4Cl were mixed and ground in an agate mortar. Thereafter, the solid mixture was transferred to a porcelain crucible with a melamine foam cover (45 × 60 × 30 m^3) and fired in a furnace at 550 °C for 3 h with a ramping rate of 5 °C min^{-1}. The UiO-66 and UiO-66/g-C_3N_4 composites were fabricated by the solvothermal method (Fig. S2†). First, H_2BDC (1.71 g) was dissolved in DMF (60 mL), whereas $ZrOCl_2 \cdot 8H_2O$ (2.52 g) and CTABr (0.356 g) were dissolved in distilled water (40 mL). Afterward, these solutions were uniformly mixed by vigorously stirring for 60 min to form a clear solution (solution A). Homogeneous suspension B was prepared by dispersing 0.8 g of g-C_3N_4 into 20 mL of distilled water under ultrasonic treatment for 30 min. Solution A was slowly added to homogeneous suspension B under vigorous stirring. After further stirring for 60 min, the mixture was placed in a Teflon-lined autoclave and heated at 100 °C for 12 h. The products were filtered and washed with DMF and ethanol to remove unreacted substances. Finally, the obtained UiO-66 and UiO-66/g-C_3N_4 composites were dried overnight in an oven at 80 °C. The obtained UiO-66/g-C_3N_4 catalysts were identified as UiO-66, UiO-66/g-C_3N_4-10%, UiO-66/g-C_3N_4-20%, UiO-66/g-C_3N_4-30%, and UiO-66/g-C_3N_4-40%, according to the weight ratios of g-C_3N_4 : 0 wt%, 10 wt%, 20 wt%, 30 wt%, and 40 wt%, respectively.

2.4 Characterization of the UiO-66 and UiO-66/g-C_3N_4

X-ray diffraction (XRD) of the UiO-66 and UiO-66/g-C_3N_4 samples was performed on a D8 Advance diffractometer (Bruker, Germany) with CuKα as the radiation source ($\lambda = 0.154$ 06 nm and a 2θ range of 2–50°). The morphology of the UiO-66 and UiO-66/g-C_3N_4 samples was characterized by scanning electron microscopy (SEM) and transmission electron microscopy (TEM) on Hitachi S4700 and Leica LEO 906E instruments, respectively. Energy-dispersive X-ray spectroscopy (EDS) was used to determine the composition of the elements in the UiO-66/g-C_3N_4 sample on a JEOL JED-2300 instrument. The elemental components were analyzed using a Thermo VG RSCAKAB 250× high-resolution X-ray photoelectron spectrometer (XPS). Surface area (S_{BET}), total pore volume (V_{pore}), and

mean Barrett–Joyner–Halenda (BJH) pore diameter were analyzed on a Tristar-3030 instrument (Micromeritics-USA) with N_2 adsorbed at −196 °C. The UiO-66 and UiO-66/g-C_3N_4 samples were degassed with N_2 gas at 150 °C for 12 h before measuring N_2 adsorption. The surface functional groups of the UiO-66 and UiO-66/g-C_3N_4 samples were analyzed on a Nicolet Nexus 670 Fourier-transform infrared (FT-IR) spectrometer. UV-vis absorption spectra, UV-vis diffuse reflectance spectra (UV-vis DRS), and photoluminescence (PL) spectra were acquired using a Shimadzu UV-2600 spectrometer, a Shimadzu UV-3100 spectrometer, and Varian, respectively.

2.5 Electrochemical measurements

The electrodes used for Mott–Schottky measurements were prepared by dispersing the powder samples in ethanol (0.1 mL: 0.05 g mL^{-1}) and placing them in a fluorine-doped tin oxide (FTO) plate (0.283 cm^2) to dry naturally at room temperature for 24 h. Thereafter, the powder samples dispersed on the FTO plates were placed in a 0.1 M Na_2SO_4 solution and applied to a voltage of 10 mV at 10 kHz. The Mott–Schottky measurements were performed in the dark over a potential range from −1.5 to +1.5 V (V *vs.* Ag/AgCl).

2.6 Photocatalytic activity

The photodegradation and hydrolysis of the DMNPs over UiO-66 and UiO-66/g-C_3N_4 were performed according to a previous report.[34,35] First, 2.5 mg (0.0015 mmol) of the UiO-66/g-C_3N_4 samples and 1 mL of water (pH = 7) were added to a 2 mL reactor and vigorously stirred at 1300 rpm. Thereafter, 4 μL (0.025 mmol) of DMNP was added to the above suspension and irradiated with 30 W pseudo-sunlight. The molar ratio of catalyst and DMNP was fixed as 6 mol%. The intensity of incident light is about 2880 Lux. The distance between the surface of the reaction solution and the light source was fixed at about 15 cm. During 60 min of irradiation, 20 μL of the mixture in the reaction system was removed at a certain time intervals and diluted with 10 mL of 0.15 M *N*-ethyl morphine solution to monitor *p*-nitrophenoxide. To evaluate the reusability of the UiO-66/g-C_3N_4-30% sample, the catalyst was washed several times with aqueous *N*-ethyl morphine, soaked in ethanol, and dried at 80 °C for 12 h to be used for the next reaction cycle. Radical scavengers, including ammonium oxalate monohydrate (AO), *tert*-butanol (TBA), potassium dichromate ($K_2Cr_2O_7$), and 1,4-benzoquinone (BQ), with a concentration of 1 mM, were employed to capture holes (h^+), hydroxyl ($^{\bullet}OH$), electrons (e^-), and superoxide anion ($^{\bullet}O_2^-$), respectively.

3 Results and discussion

3.1 Structure and morphology characterization of the UiO-66 and UiO-66/g-C_3N_4 composites

The crystalline structure of the UiO-66 and UiO-66/g-C_3N_4 composites was investigated by XRD analysis. The powder XRD patterns of the UiO-66 and UiO-66/g-C_3N_4composites (Fig. 1A and S3†) showed eight main diffraction peaks at 2θ of 7.2°, 8.3°, 12°, 17°, 22°, 26°, 31°, and 44°, corresponding to the reflection planes of (111), (200), (022), (004), (044), (006), (117) and (339) of UiO-66 (Zr) (CCDC No. 733458), respectively.[8,36,37] Additionally, the characteristic peak of the g-C_3N_4 phase was detected at 27.3° (JCPDS No. 87-1526) (Fig. 1A),[38] implying that the UiO-66/g-C_3N_4 composites were produced. Further, we observed that the intensity of the peak at 27.3° increased when the g-C_3N_4 content in the composites increased from 10 to 40 wt%. These outcomes indicated that the addition of g-C_3N_4 did not affect the structure of the UiO-66 material.

The FTIR spectra of the UiO-66 and UiO-66/g-C_3N_4 samples (Fig. 1B) were obtained to investigate the composition of the UiO-66 and UiO-66/g-C_3N_4 samples. The vibrations at 3200 to 3600 cm^{-1} were attributed to the –OH of water molecules that were physically adsorbed inside the capillaries of the UiO-66 or g-C_3N_4 materials.[39] The band oscillations at 1583, 1437, and 1388 cm^{-1} were assigned to the asymmetrical stretching and symmetrical stretching variations of the carboxyl groups.[36] The bands at 746 cm^{-1} and 661 cm^{-1} were assigned to the Z–O stretching oscillations.[11] In the FTIR spectrum of g-C_3N_4 (Fig. 1B), the bands at 1254, 1320, and 1456 cm^{-1} were related to aromatic g-C_3N_4 stretching,[40] while the bands at 1574 and 1638 cm^{-1} were attributed to the of C=N bond.[41] However, the absence of these fluctuations in the FTIR spectra of the UiO-66/

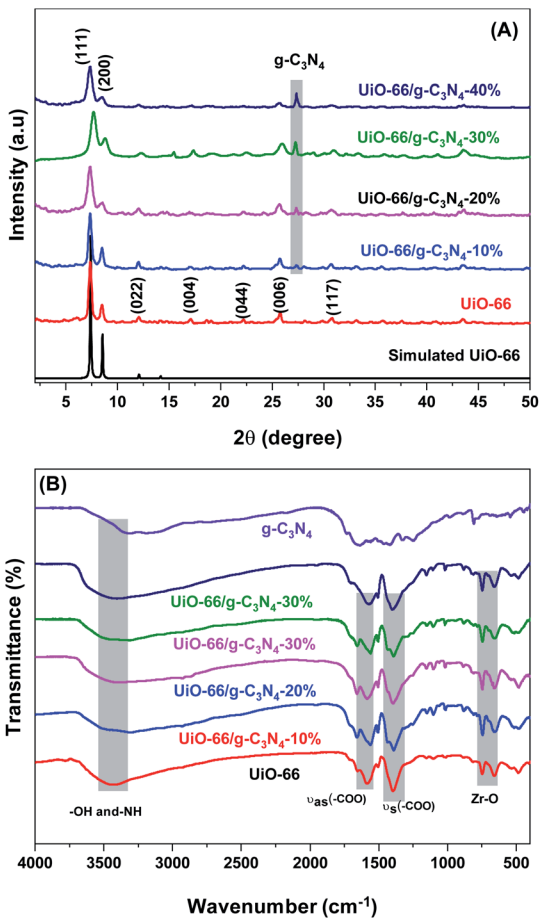

Fig. 1 (A) XRD patterns and (B) FT-IR spectra of UiO-66 and UiO-66/g-C_3N_4 composites.

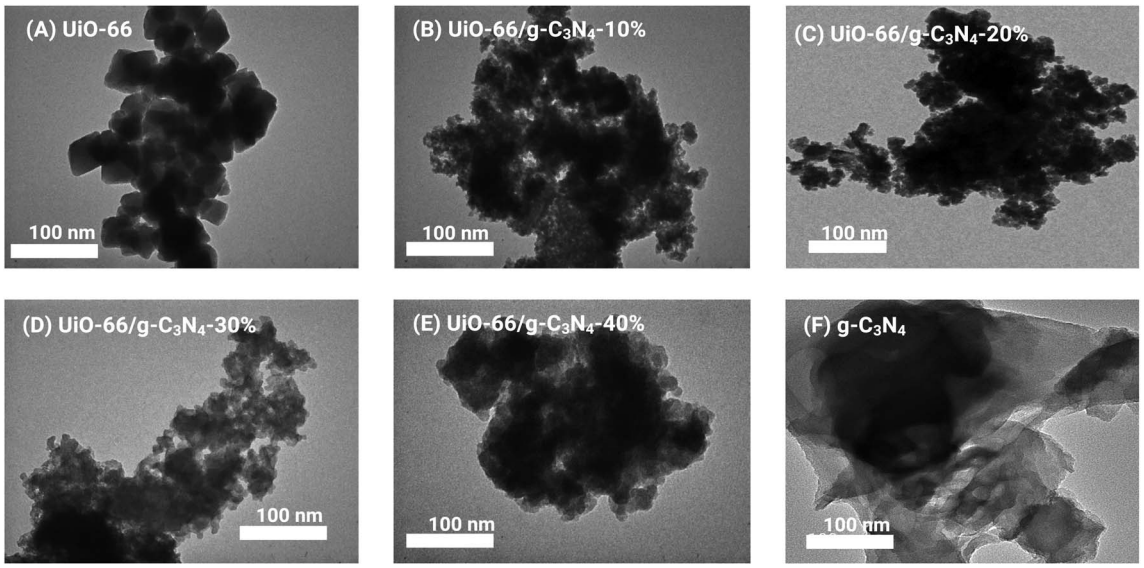

Fig. 2 TEM images of UiO-66 (A), UiO-66/g-C_3N_4-10% (B), UiO-66/g-C_3N_4-20% (C), UiO-66/g-C_3N_4-30% (D), UiO-66/g-C_3N_4-40% (E) composites and g-C_3N_4 (F).

g-C_3N_4 composites (Fig. 1B) may be due to the overlapping of the bands in the UiO-66 sample.

The SEM and TEM images of UiO-66showed nanoparticles with a diameter of 80–120 nm, while g-C_3N_4 plates with un-uniform length were observed in the SEM and TEM images of g-C_3N_4 (Fig. S4† and 2). For the UiO-66/g-C_3N_4 samples, as shown in the TEM image (Fig. 2), there were dark areas on the micrograph of the MOF nanocrystals mounted on top of the g-C_3N_4 plates, and the relatively light contours corresponded to the g-C_3N_4 sheets decorated with UiO-66 nanoparticles. Similarly, the SEM image of the UiO-66/g-C_3N_4-40% sample showed that there was a clustering of the UiO-66 nanoparticles into large particles of 100–150 nm (Fig. S4†).

The chemical composition of the UiO-66 and UiO-66/g-C_3N_4-30% samples was analyzed by EDS. The EDS (Fig. S5†) and EDS-mapping spectra (Fig. 3) confirmed the presence and uniform distribution of C, O, Zr, and N throughout the composites. Further, the mass ratios of C, O, and Zr decreased in sample UiO-66/g-C_3N_4%, while the N content increased by 17.22 wt% (Table S1†). The N content accounted for 17.22 wt% in sample UiO-66/g-C_3N_4-30%, showing that the weight ratio of the g-C_3N_4/UiO-66 determined by EDS was considerably close to the estimated value of 30%.

The porosity properties of the UiO-66 and UiO-66/g-C_3N_4 samples were obtained by N_2 adsorption–desorption isotherms and pore size distributions (Fig. 4). The UiO-66/g-C_3N_4 samples exhibited a type IV isotherm with hysteresis upon desorption in the P/P_o of 0.45–1, presenting typical mesoporous materials.[42] However, UiO-66 exhibited a type I isotherm with an existing micro-sized pore.[43] The UiO-66 sample had the highest estimated S_{BET} (1440 $m^2\ g^{-1}$) and V_{pore} value (1.05 $cm^3\ g^{-1}$) and the smallest pore diameter (3.44 nm) (Table 1). The UiO-66/g-C_3N_4 samples had a surface area of 583–1162 $m^2\ g^{-1}$, pore volume of 0.79–1.49 $cm^3\ g^{-1}$, and an average pore diameter of 4.08–5.56 nm (Table 1). Thus, the addition of the g-C_3N_4 in the UiO-66 sample, UiO-66/g-C_3N_4 samples, significantly reduced the surface area compared to the pure UiO-66 sample. However, because of the expansion of the pore diameter from 3.44 to

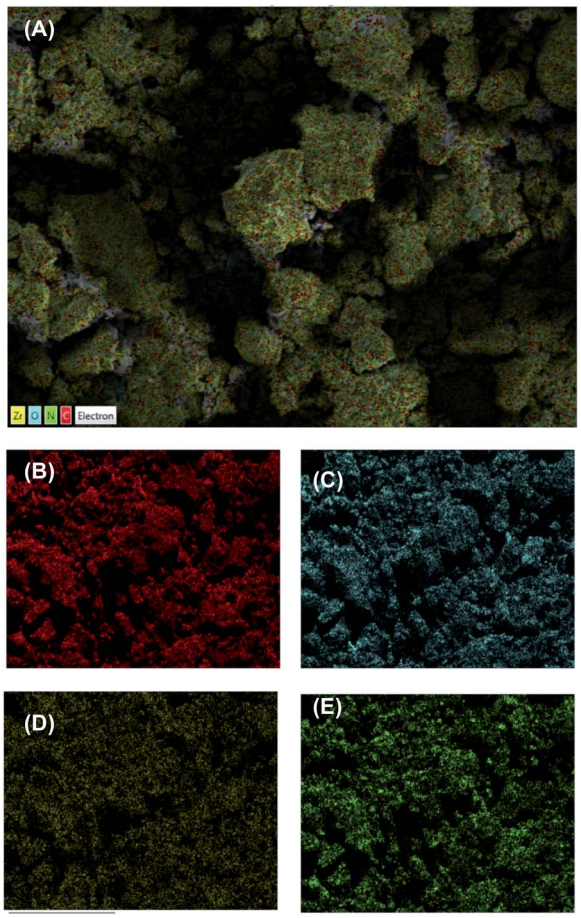

Fig. 3 EDS mapping element layered image (A), EDS element mapping images of C (B), O (C), Zr (D) and N (E) of UiO-66/g-C_3N_4-30% sample.

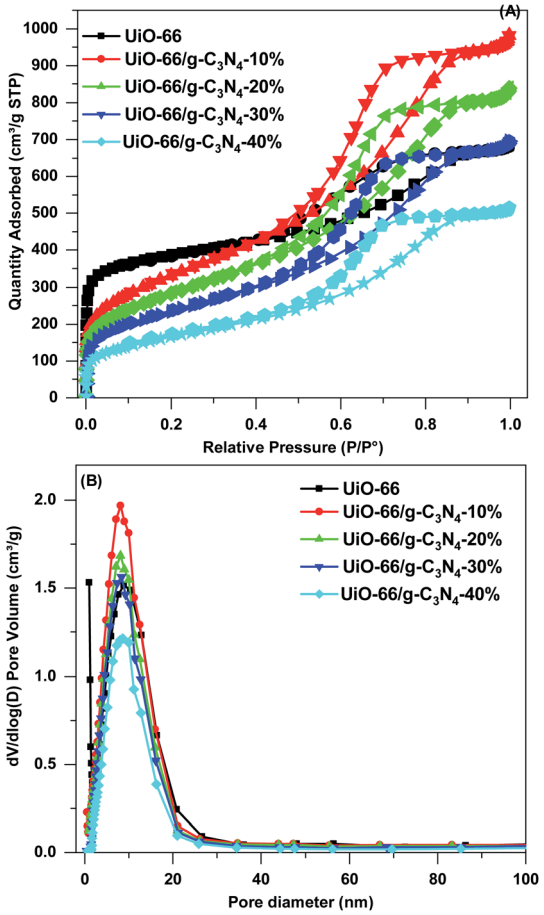

Fig. 4 (A) N_2 adsorption–desorption isotherms and (B) pore size distributions of UiO-66 and UiO-66/g-C_3N_4 composite.

4.08 nm, the total pore volume increased from 1.05 to 1.49 $cm^3 g^{-1}$ (Table 1). The pore volume and pore diameter significantly increased, favoring the adsorption and degradation of DMNP because the Zr_6 metal sites expanded the decomposition reaction.[44] Furthermore, the addition of the g-C_3N_4 helped to generate more defects, which improved the degradation performance of the catalyst.[45]

The chemical states and surface compositions of the UiO-66 and UiO-66/g-C_3N_4-30% samples were analyzed by XPS (Fig. 5). The full-scan XPS spectra of UiO-66 (Fig. 5A) showed peaks of C 1s (285.6 eV), O 1s (532.6 eV), and Zr (184.6 eV). Similarly, the full-scan XPS spectra of the UiO-66/g-C_3N_4-30% sample (Fig. 5B) showed peaks of C 1s (285.5 eV), O 1s (531.8 eV), Zr (183.7 eV), and N 1s (401.7 eV).[46] The C 1s spectra of the UiO-66 sample showed four peaks with binding energies at 282.52, 284.07, 286.53, and 290.02 eV, which were assigned to C=C/C–C, C–O, C=O, and O–C=O groups, respectively (Fig. 5C).[32,47] The C 1s spectra of the UiO-66/g-C_3N_4-30% sample (Fig. 5D) showed six peaks and their binding energies at C=C/C–C (281.74 eV), C–O (283.78 eV), C=O (286.73 eV), O–C=O (288.70 eV), sp^2 bonded carbon (N–C=N, 286.23 eV), and graphite carbon group (sp^3 C, 282.34 eV).[32] The high-resolution O 1s XPS spectra of the UiO-66 sample (Fig. 5E) showed that three peaks at 530.81, 532.35, and 533.53 eV were attached to the O in the metal-bonded crystal lattice (Zr–O), the chemisorbed O, and the O in group O–C=O.[48] The O 1s spectra of the UiO-66/g-C_3N_4-30% sample (Fig. 5F) showed that three peaks at 530.69, 531.99, and 533.25 eV were attached to the O in the metal-bound crystal lattice (Zr–O), chemisorbed O species, and O in the O–C=O group.[48] The high-resolution spectrum Zr 3d of the UiO-66 sample (Fig. 5G) showed signals at 182.88 and 185.19 eV related to Zr $3d_{5/2}$ and Zr $3d_{3/2}$, respectively. The high-resolution spectra Zr 3d of the UiO-66 sample (Fig. 5H) showed signals at 181.92 and 184.75 eV related to Zr $3d_{5/2}$ and Zr $3d_{3/2}$, respectively.[49] The N 1s spectra of the g-C_3N_4 sample (Fig. 5K) showed three peaks attached to the binding energy sp^2 N (C–N=C, 399.25 eV), tertiary N atom (sp^3 N, 400.42 eV), and amine functional group (C_2–NH, 402.25 eV).[50] The high-resolution O 1s and Zr 3d XPS spectra of the UiO-66/g-C_3N_4-30% sample shifted to a lower binding energy region than that of the UiO-66 sample; this was due to the shift in the electron from g-C_3N_4 to UiO-66.[50]

Table 1 Textual characteristics and energy gap-band (E_g) of g-C_3N_4, UiO-66, and UiO-66/g-C_3N_4 samples

Samples	S_{BET} ($m^2 g^{-1}$)	V ($cm^3 g^{-1}$)	D_{BJH} (nm)	E_g (eV)
UiO-66	1440	1.05	3.44	3.50
UiO-66/g-C_3N_4-10%	1162	1.49	4.08	3.28
UiO-66/g-C_3N_4-20%	994	1.28	4.99	3.11
UiO-66/g-C_3N_4-30%	827	1.06	5.32	2.91
UiO-66/g-C_3N_4-40%	583	0.79	5.56	2.82

3.2 The optical and electrochemical performances

The optical properties of the g-C_3N_4, UiO-66 and UiO-66/g-C_3N_4 composites were analyzed by UV-vis DRS (Fig. 6A). The maximum light absorption boundary of UiO-66 appeared in the UV range (380 nm), whereas the absorption edge of the UiO-66/g-C_3N_4 and g-C_3N_4 samples appeared in the visible region (450–550 nm). This outcome indicates that the *in situ* hydrothermal synthesis of the UiO-66 sample onto the g-C_3N_4 sheets increased the visible light absorption capacity of the UiO-66/g-C_3N_4 materials. The bandgap energy (E_g) of the g-C_3N_4, UiO-66, and UiO-66/g-C_3N_4 samples were estimated using a Tauc plot. The E_g values of the UiO-66 and g-C_3N_4 samples were 3.5 and 2.72 eV, respectively (Fig. 6B and Table 1). The E_g values of the UiO-66/g-C_3N_4samples were 2.82–3.28 eV (Fig. 6B and Table 1). The conduction band potentials (E_{CB}) of the g-C_3N_4, UiO-66, and UiO-66/g-C_3N_4-30 samples were determined by the Mott–Schottky plots (Fig. 6C). The E_{CB} values of g-C_3N_4, UiO-66, and UiO-66/g-C_3N_4-30% were found to be −0.91, −0.66 and 0.78 eV, respectively. The valence band positions (E_{VB}) can be estimated based on the relation between the E_g and E_{CB} (eqn (1)):

$$E_{VB} = E_g + E_{CB} \quad (1)$$

The E_{VB} value of g-C_3N_4, UiO-66, and UiO-66/g-C_3N_4-30% were estimated to be 1.81, 2.84 and 2.13 eV, respectively. The PL spectra were used to evaluate the effect of g-C_3N_4 on the recombination process of the hole and electron pairs in the UiO-

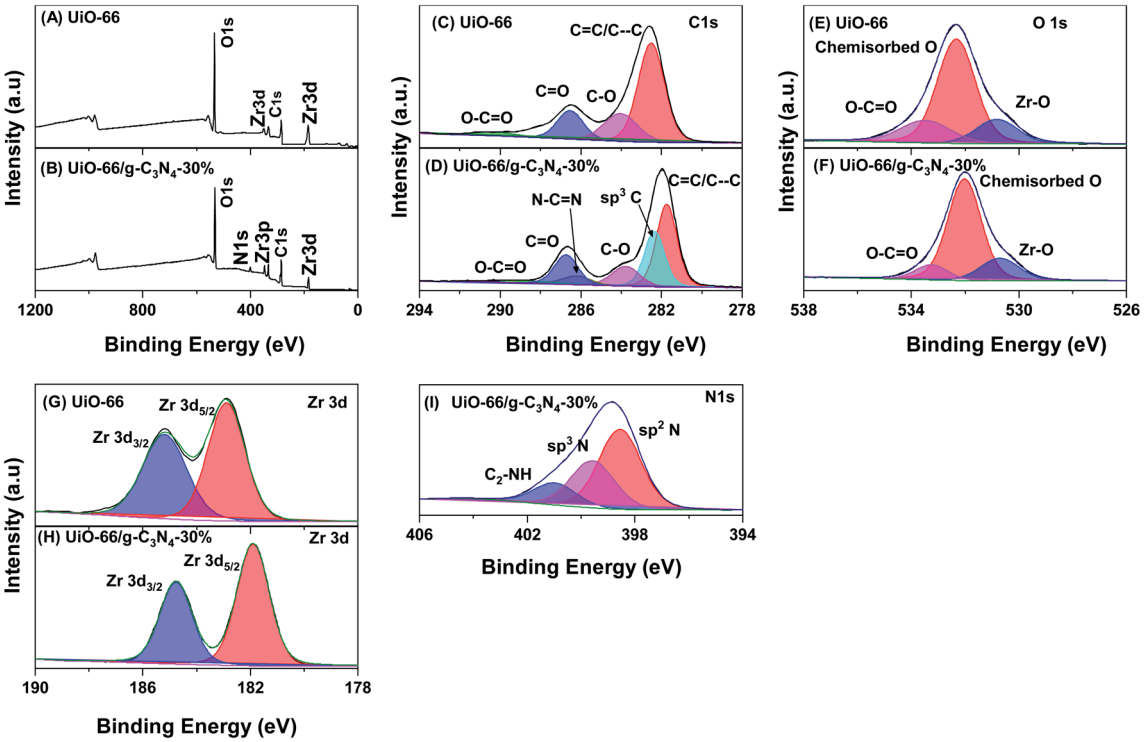

Fig. 5 XPS survey spectra of UiO-66 (A) and UiO-66/g-C_3N_4-30% (B); high-resolution C 1s XPS spectra of UiO-66 (C) and UiO-66/g-C_3N_4-30% (D); high-resolution O 1s XPS spectra of UiO-66 (E) and UiO-66/g-C_3N_4-30% (F); high-resolution Zr 3d XPS spectra of UiO-66 (G) and UiO-66/g-C_3N_4-30% (H); high-resolution N 1s XPS spectra of UiO-66/g-C_3N_4-30% (I).

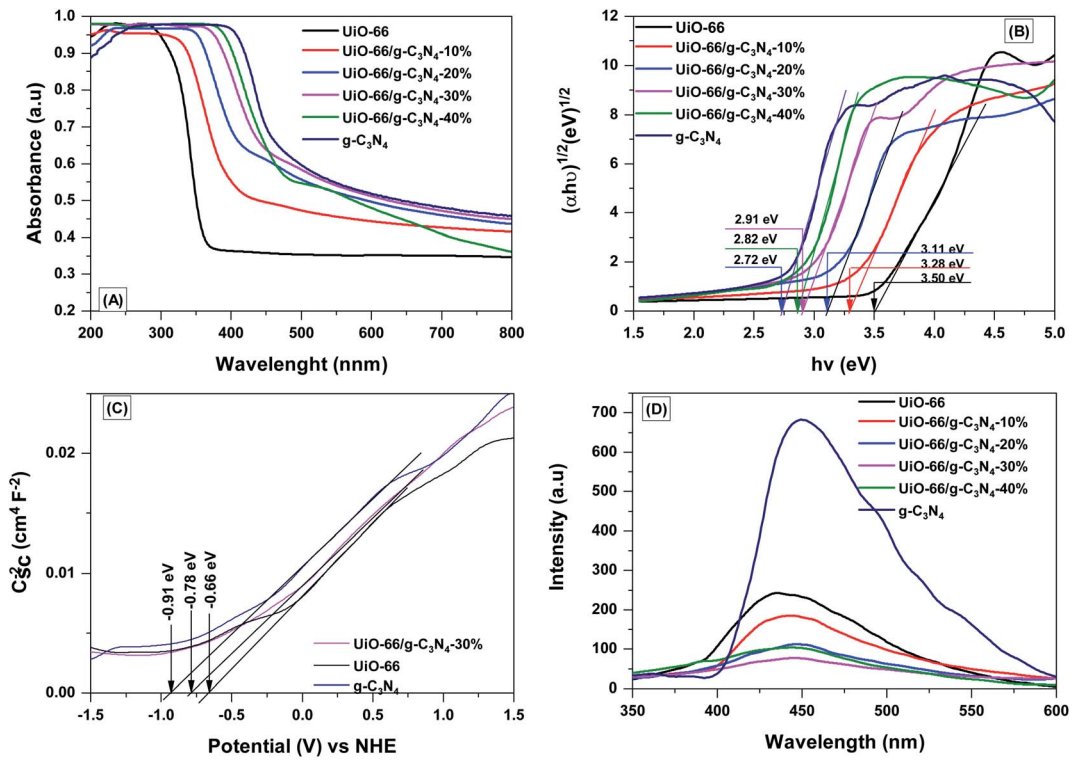

Fig. 6 UV-vis diffuse reflectance spectra (A), band-gap energies (B), Mott–Schottky plot (C) and photoluminescence spectra (D) of g-C_3N_4, UiO-66 and UiO-66/g-C_3N_4 composites.

66, g-C_3N_4, and UiO-66/g-C_3N_4 materials (Fig. 6D). The g-C_3N_4 sample showed an intense emission peak at 442 nm because of the electron–hole recombination and n–π* electron transition.[39] Meanwhile, sample UiO-66 had an emission peak at 440 nm because of the recombination of the electron and hole pairs.[25] The emission intensity at 440 nm was significantly reduced after applying UiO-66 to the g-C_3N_4 sheets; the recombination of the electron and hole pairs in the material was reduced by the electron capture of g-C_3N_4 by the UiO-66 material. The PL intensity of the samples decreased in the following order: g-C_3N_4 > UiO-66 > UiO-66/g-C_3N_4-10% > UiO-66/g-C_3N_4-30% > UiO-66/g-C_3N_4-20% > UiO-66/g-C_3N_4-30%.

3.3 Photocatalytic performances

The photocatalytic activity of the UiO-66 and UiO-66/g-C_3N_4 samples was evaluated by the decomposition of DMNP under visible light irradiation (Fig. 7A). The DMNP treatment efficiency over the g-C_3N_4 photocatalyst reached 28.2% after 60 min of irradiation. Meanwhile, catalyst UiO-66 achieved a DMNP degradation efficiency of 54.65% after 60 min of reaction. Notably, the DMNP removal efficiency over the UiO-66/g-C_3N_4 samples was significantly enhanced compared with that of bare g-C_3N_4 or UiO-66. The DMNP removal efficiency over the UiO-66/g-C_3N_4 samples increased from 86.84% to 98.55% with increasing g-C_3N_4 content from 10 to 30 wt%. However, when the g-C_3N_4 content increased to 40 wt%, the DMNP treatment efficiency decreased from 98.55% to 91.56%, which was due to the significant reduction in surface area and capillary volume (Table 1). The significant increase in the DMNP processing efficiency of the UiO-66/g-C_3N_4 samples was attributed to the enhancement of visible light absorption, as confirmed by the UV-vis DRS and PL results (Fig. 7 and Table 1). Moreover, the pore size of the UiO-66/g-C_3N_4 samples was improved, making the phase contact of reactants more favorable instead of the contact between the catalysts and the phosphate ester linkage, which occurs only on the outer surface of the catalyst.[3] Additionally, the UiO-66/g-C_3N_4 samples contained acidic Lewis octahedral Zr6 oxo clusters that cleaved the phosphate ester bond to yield dimethyl phosphate and 4-nitrophenol (Fig. S6†).[11]

Further, the effect of the photocatalyst dose on the photocatalytic activity of the UiO-66/g-C_3N_4-30% sample was investigated. When the amount of the UiO-66/g-C_3N_4-30% sample increased from 2 to 10 mol%, the degradation rate of the DMNP significantly increased from 84.1% to 98.9% after 60 min of light irradiation (Fig. 7B). This increase may be due to the uniform dispersion of the catalyst in a solution, which significantly increased the contact between the DMNP molecules and the active sites of the catalyst.[24,48] When increasing the catalyst dose from 12 mol%, the rate of the DMNP degradation reaction slightly increased. Thus, with a catalytic mass of 2, 4, 6, 8, and 12 mol%, the half-life of DMNP was 11.89, 6.95, 4.67, 2.38, and 2.17 min, respectively.

The kinetic curve of the adsorption and degradation of the DMNP by the UiO-66 and UiO-66/g-C_3N_4-30% samples are shown in Fig. 7C. In the dark, the UiO-66 and UiO-66/g-C_3N_4-30% samples exhibited a low DMNP removal by adsorption

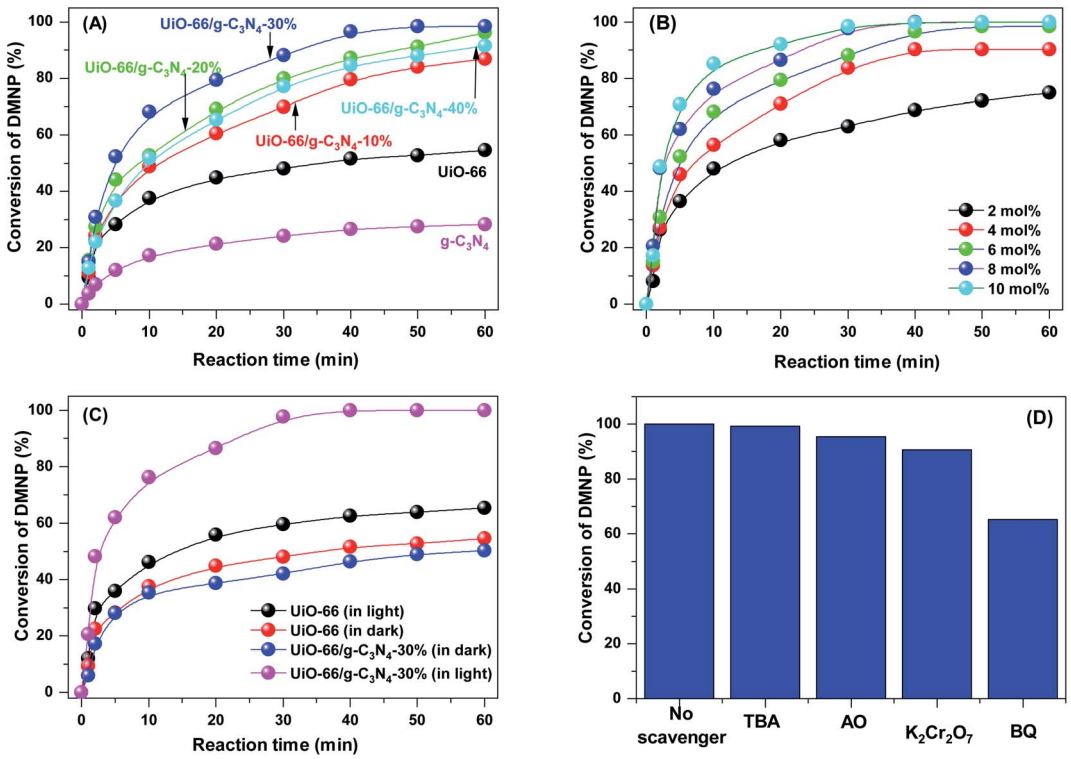

Fig. 7 The conversion of DMNP as a function of reaction time over g-C_3N_4, UiO-66, and UiO-66/g-C_3N_4 samples (A), effect of different UiO-66/g-C_3N_4-30% catalysts does on the conversion of DMNP (B); the conversion of DMNP under dark and lighting conditions under dark and lighting conditions over UiO-66 and UiO-66/g-C_3N_4-30% (C) and active species trapping experiments (D).

(≈50%); this was because of the number of octahedral Zr6 oxo clusters of the UiO-66/g-C_3N_4-30% model was lower than that of UiO-66 (Table S1†). After 60 min of irradiation, the degradation rate of DMNP over UiO-66/g-C_3N_4-30% significantly increased to 98.9%, indicating the resonant light absorption effect between UiO-66 and g-C_3N_4. The DMNP removal rate over UiO-66 slightly increased under light irradiation because the UiO-66 catalyst had poor visible light absorption.[51]

The half-life of the DMNP based on previously published heterogeneous catalysts is presented in Table S2.† The shortest half-life of 1.6 min was reported by Song *et al.*[8] However, DMNP removal reactions are conventionally performed in 0.45 M *N*-ethylmorpholine buffer (pH of 10) to speed up DMNP removal. Daniel Bůžek *et al.*[9] used UiO-66 to hydrolyze DMNPs at a pH of 7, showing that the half-life of DMNP was 7 min. In this study, the heterogeneous catalyst, UiO-66/g-C_3N_4, degraded DMNP with a half-life of 2.38 min, which indicates that UiO-66/g-C_3N_4 is a fast DMNP-removing photocatalyst.

The UV-vis spectra of DMNP (Fig. S7†) in water showed that the wavelength intensity at 280 nm decreased because of the decomposition of the DMNP, and the wavelength intensity at 403 nm increased because of the formation of a hydrolysis product, 4-nitrophenoxide. Fig. S8† shows that DMNP was mixed with 0.15 M *N*-ethylmorpholine buffer, and with increasing sunlight irradiation time, the color of the transparent solution gradually changed to pale yellow.

The LC-MS spectra of the UiO-66 sample (Fig. S9A†) showed that the products of the hydrolysis of DMNPs in water (pH of 7) included dimethyl phosphate (*m*/*z* of 126.08), methyl phosphate (*m*/*z* of 109.24), 4-nitrophenol (*m*/*z* of 137.80), and methyl 4-nitrophenyl phosphate (*m*/*z* of 231.77). Notably, methyl 4-nitrophenyl phosphate is more toxic than the DMNP.[2] The LC-MS spectra of the UiO-66/g-C_3N_4-30% sample (Fig. S9B†) showed that the products of the photocatalysis and hydrolysis of DMNPs were mainly dimethyl phosphate (*m*/*z* of 126.12), methyl phosphate (*m*/*z* of 109.23), and 4-nitrophenol (*m*/*z* of 137.83). This result showed that the degradation of DMNPs by the combination of hydrolysis and photocatalysis afforded less-toxic products than conventional hydrolysis in aqueous media. Additionally, the products of hydrolysis and photocatalysis can oxidize these organic compounds to CO_2 and H_2O.

The stability of the UiO-66/g-C_3N_4-30% sample was confirmed by repeating the DMNP removal reaction for five catalytic regenerations (Fig. S10†). The DMNP removal efficiency remained unchanged after five reaction cycles, indicating that the photocatalytic activity of the UiO-66/g-C_3N_4-30% sample was highly stable. The stability of UiO-66/g-C_3N_4-30% was further confirmed by the XRD results because no noticeable difference was found between the XRD patterns of UiO-66/g-C_3N_4-30% before and after reaction (Fig. S11†).

3.4 Mechanism of the photocatalytic reaction

To determine the role of free radicals in the DMNP removal efficiency, reactive radical trapping experiments were performed. Radical scavengers, including AO, TBA, $K_2Cr_2O_7$, and BQ, were employed to capture h^+, $^{\cdot}OH$, e^- and $^{\cdot}O_2^-$, respectively.[52] As shown in Fig. 7D, the degradation rate of DMNPs was strongly influenced by AO and BQ, indicating that the h^+ and $^{\cdot}O_2^-$ radicals had a strong influence on the degradation of DMNP. Meanwhile, TBA and $K_2Cr_2O_7$ slightly decreased the removal rate of DMNPs. Thus, $^{\cdot}O_2^-$ radicals play an essential role in the degradation of DMNP. Based on the UV-vis DRS and Mott–Schottky plots measurements above, we analyzed the band structure of the g-C_3N_4, UiO-66 and UiO-66/g-C_3N_4 samples (Fig. 8A). The E_{CB} values of g-C_3N_4, UiO-66 and UiO-66/g-C_3N_4-30% were estimated to be −0.91, −0.66 and −0.78 eV, respectively, which can produce $^{\cdot}O_2^-$ radicals because the CB positions of the samples were more negative than the redox potential of $O_2/^{\cdot}O_2^-$ (−0.33 eV). The $^{\cdot}OH$ radicals can be generated on the surface of UiO-66 because the VB position of UiO-66 (+2.48 eV) was more positive than the standard potential of $^{\cdot}OH/H_2O$ (+2.40 eV). For the g-C_3N_4 sample, $^{\cdot}OH$ radicals cannot be generated on the surface of g-C_3N_4 because the VB position of g-C_3N_4 (+1.81 eV) was less than the standard potential of $^{\cdot}OH/H_2O$.

Based on previous studies[16,26–28] and an experimental database, we proposed the photocatalytic mechanism of sample UiO-66/g-C_3N_4, as illustrated in Fig. 8B. The heterojunction catalyst UiO-66/g-C_3N_4 was formed by light integration between UiO-66 and g-C_3N_4 with the appropriate CB and VB sites. Under solar light irradiation, a heterojunction was formed between UiO-66 and g-C_3N_4. First, when the g-C_3N_4 and UiO-66 catalysts

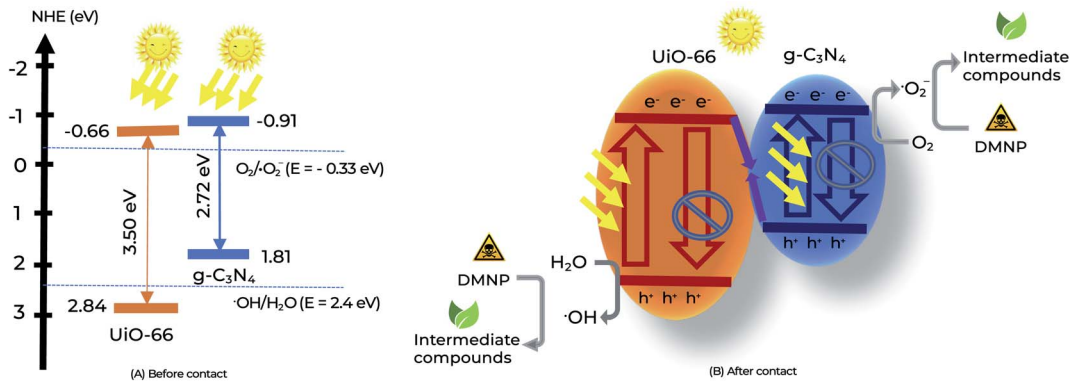

Fig. 8 The schematic of the separation and transfer of photogenerated charges over UiO-66/g-C_3N_4 before contact (A) and after contact (B).

were exposed to a light source greater than the bandgap energy of the material, the e^- moved from CB binding to VB binding to form e^- in CB and h^+ in VB as reducing and oxidizing agents, respectively, (eqn (2)).

$$\text{UiO-66/g-}C_3N_4 + h\nu \rightarrow \text{UiO-66/g-}C_3N_4\ (h^+ + e^-) \quad (2)$$

Thereafter, the e^- in the CB of UiO-66 recombined with the h^+ in the VB of g-C_3N_4. The e^- in CB of g-C_3N_4 reacted with the O_2 adsorbed on the surface of g-C_3N_4 to generate $^{\bullet}O_2^-$ radicals (eqn (3)).

$$\text{g-}C_3N_4\ (e^-) + O_2 \rightarrow {}^{\bullet}O_2^- \quad (3)$$

Besides, the h^+ in the VB position of UiO-66 reacted with H_2O to form $^{\bullet}OH$ radicals (eqn (4)).

$$\text{UiO-66}\ (h^+) + H_2O \rightarrow {}^{\bullet}OH + H^+ \quad (4)$$

Finally, the radicals, such as $^{\bullet}O_2^-$, h^+, and $^{\bullet}OH$, oxidized the DMNP molecule to afford less-toxic products (eqn (5)).

$$^{\bullet}OH\ (\text{or/and } h^+ \text{ and } {}^{\bullet}O_2^-) + \text{DMNP} \rightarrow \text{production} \quad (5)$$

4 Conclusions

UiO-66 was successfully synthesized using an H_2BDC linker obtained from waste plastic. Afterward, this material was combined with g-C_3N_4 to form a p–n UiO-66/g-C_3N_4 heterojunction composite as an effective photocatalyst for the conversion of DMNP to non-toxic compounds. The UiO-66/g-C_3N_4 material exhibited a high surface area (1440 $m^2\ g^{-1}$) and a high capillary volume (1.49 $cm^3\ g^{-1}$). Additionally, the as-developed UiO-66/g-C_3N_4 heterojunction composite enhanced the ability to harvest visible light and restrict the recombination of photogenerated electrons and holes. This outcome was presented by UV-vis DRS, PL, and photoelectrochemical test data. Further, compared to the bare UiO-66 and g-C_3N_4, the UiO-66/g-C_3N_4 samples exhibited the rapid oxidation degradation of DMNP with a short half-life ($t_{1/2}$ of 2.17 min) under mild conditions. Our study is expected to shed light on the design of more efficient MOF-based catalysts for the conversion of CWAs to non-toxic compounds.

Author contributions

Dung Van Le: writing – original draft, methodology, data curation. Manh B. Nguyen: writing – original draft, data curation, visualization. Phuong T. Dang: writing – review & editing, supervision. Taeyoon Lee: writing – review & editing, methodology, formal analysis. Trinh Duy Nguyen: conceptualization, writing – review & editing, supervision.

Conflicts of interest

There are no conflicts to declare.

Acknowledgements

This research is funded by Graduate University of Science and Technology under Grant Number GUST.STS.ĐT2019-HH04.

References

1 I. M. Raju, T. S. Rao, K. V. D. Lakshmi, M. R. Chandra, J. S. Padmaja and G. Divya, *J. Environ. Chem. Eng.*, 2019, **7**, 103211.
2 C. Wilson, N. J. Cooper, M. E. Briggs, A. I. Cooper and D. J. Adams, *Org. Biomol. Chem.*, 2018, **16**, 9285–9291.
3 M. J. Katz, J. E. Mondloch, R. K. Totten, J. K. Park, S. T. Nguyen, O. K. Farha and J. T. Hupp, *Angew. Chem., Int. Ed.*, 2014, **53**, 497–501.
4 A. Yao, X. Jiao, D. Chen and C. Li, *ACS Appl. Mater. Interfaces*, 2020, **12**, 18437–18445.
5 J. Dong, J. Hu, Y. Chi, Z. Lin, B. Zou, S. Yang, C. L. Hill and C. Hu, *Angew. Chem., Int. Ed.*, 2017, **56**, 4473–4477.
6 M. C. de Koning, M. van Grol and T. Breijaert, *Inorg. Chem.*, 2017, **56**, 11804–11809.
7 Y. Hou, H. An, Y. Zhang, T. Hu, W. Yang and S. Chang, *ACS Catal.*, 2018, **8**, 6062–6069.
8 L. Song, T. Zhao, D. Yang, X. Wang, X. Hao, Y. Liu, S. Zhang and Z.-Z. Yu, *J. Hazard. Mater.*, 2020, **393**, 122332.
9 D. Bůžek, J. Demel and K. Lang, *Inorg. Chem.*, 2018, **57**, 14290–14297.
10 R. Gil-San-Millan, E. López-Maya, M. Hall, N. M. Padial, G. W. Peterson, J. B. DeCoste, L. M. Rodríguez-Albelo, J. E. Oltra, E. Barea and J. A. R. Navarro, *ACS Appl. Mater. Interfaces*, 2017, **9**, 23967–23973.
11 R. Gil-San-Millan, E. López-Maya, A. E. Platero-Prats, V. Torres-Pérez, P. Delgado, A. W. Augustyniak, M. K. Kim, H. W. Lee, S. G. Ryu and J. A. R. Navarro, *J. Am. Chem. Soc.*, 2019, **141**, 11801–11805.
12 H.-B. Luo, A. J. Castro, M. C. Wasson, W. Flores, O. K. Farha and Y. Liu, *ACS Catal.*, 2021, **11**, 1424–1429.
13 N. Iqbal, A. Afzal, I. Khan, M. S. Khan and A. Qurashi, *Sci. Rep.*, 2021, **11**, 16886.
14 A. K. Singh, N. Jaiswal, R. K. Gautam and I. Tiwari, *J. Electroanal. Chem.*, 2021, **887**, 115170.
15 J. L. Silva, B. Brena and C. M. Araujo, *J. Phys. Chem. C*, 2020, **124**, 8726–8735.
16 F. Chang, Y. Xie, C. Li, J. Chen, J. Luo, X. Hu and J. Shen, *Appl. Surf. Sci.*, 2013, **280**, 967–974.
17 L. Liu, H. Huang, Z. Chen, H. Yu, K. Wang, J. Huang, H. Yu and Y. Zhang, *Angew. Chem., Int. Ed.*, 2021, **60**, 18303–18308.
18 F. Chen, Z. Ma, L. Ye, T. Ma, T. Zhang, Y. Zhang and H. Huang, *Adv. Mater.*, 2020, **32**, 1908350.
19 S. Wang, X. Han, Y. Zhang, N. Tian, T. Ma and H. Huang, *Small Struct.*, 2021, **2**, 2000061.
20 J. Wen, J. Xie, X. Chen and X. Li, *Appl. Surf. Sci.*, 2017, **391**, 72–123.
21 M. Ismael and Y. Wu, *Sustainable Energy Fuels*, 2019, **3**, 2907–2925.
22 T. Wang, C. Nie, Z. Ao, S. Wang and T. An, *J. Mater. Chem. A*, 2020, **8**, 485–502.

23 A. Naseri, M. Samadi, A. Pourjavadi, A. Z. Moshfegh and S. Ramakrishna, *J. Mater. Chem. A*, 2017, **5**, 23406–23433.
24 X. N. Pham, H. T. Nguyen, T. N. Pham, T.-T.-B. Nguyen, M. B. Nguyen, V. T.-T. Tran and H. V. Doan, *J. Taiwan Inst. Chem. Eng.*, 2020, **114**, 91–102.
25 M. Hassannezhad, M. Hosseini, M. R. Ganjali and M. Arvand, *Anal. Methods*, 2019, **11**, 2064–2071.
26 G. Liao, C. Li, X. Li and B. Fang, *Cell Rep. Phys. Sci.*, 2021, **2**, 100355.
27 G. Liao, Y. Gong, L. Zhang, H. Gao, G.-J. Yang and B. Fang, *Energy Environ. Sci.*, 2019, **12**, 2080–2147.
28 G. Liao, C. Li, S. Y. Liu, B. Fang and H. Yang, *Trends Chem.*, 2022, **4**, 111–127.
29 L. Jiang, X. Yuan, Y. Pan, J. Liang, G. Zeng, Z. Wu and H. Wang, *Appl. Catal., B*, 2017, **217**, 388–406.
30 Y. Li, Y. Fang, Z. Cao, N. Li, D. Chen, Q. Xu and J. Lu, *Appl. Catal., B*, 2019, **250**, 150–162.
31 Y. Zhou, W. Lv, B. Zhu, F. Tong, J. Pan, J. Bai, Q. Zhou and H. Qin, *ACS Sustainable Chem. Eng.*, 2019, **7**, 5801–5807.
32 X. Zhang, Y. Yang, W. Huang, Y. Yang, Y. Wang, C. He, N. Liu, M. Wu and L. Tang, *Mater. Res. Bull.*, 2018, **99**, 349–358.
33 J. H. Zhang, Y. J. Hou, S. J. Wang, X. Zhu, C. Y. Zhu, Z. Wang, C. J. Li, J. J. Jiang, H. P. Wang, M. Pan and C. Y. Su, *J. Mater. Chem. A*, 2018, **6**, 18252–18257.
34 J. E. Mondloch, M. J. Katz, W. C. Isley III, P. Ghosh, P. Liao, W. Bury, G. W. Wagner, M. G. Hall, J. B. DeCoste, G. W. Peterson, R. Q. Snurr, C. J. Cramer, J. T. Hupp and O. K. Farha, *Nat. Mater.*, 2015, **14**, 512–516.
35 C. Hu, W.-F. Tsai, W.-H. Wei, K.-Y. A. Lin, M.-T. Liu and K. Nakagawa, *Carbon*, 2021, **175**, 467–477.
36 Z. S. Moghaddam, M. Kaykhaii, M. Khajeh and A. R. Oveisi, *Spectrochim. Acta, Part A*, 2018, **194**, 76–82.
37 J. H. Cavka, S. Jakobsen, U. Olsbye, N. Guillou, C. Lamberti, S. Bordiga and K. P. Lillerud, *J. Am. Chem. Soc.*, 2008, **130**, 13850–13851.
38 N. Tian, H. Huang and Y. Zhang, *Appl. Surf. Sci.*, 2015, **358**, 343–349.
39 N. T. Dung, N. V. Hiep, M. B. Nguyen, V. D. Thao and N. N. Huy, *Korean J. Chem. Eng.*, 2021, **38**, 2034–2046.
40 R. Ye, H. Fang, Y.-Z. Zheng, N. Li, Y. Wang and X. Tao, *ACS Appl. Mater. Interfaces*, 2016, **8**, 13879–13889.
41 J. Ma, Q. Yang, Y. Wen and W. Liu, *Appl. Catal., B*, 2017, **201**, 232–240.
42 M. D. Donohue and G. L. Aranovich, *Adv. Colloid Interface Sci.*, 1998, **76–77**, 137–152.
43 N. Assaad, G. Sabeh and M. Hmadeh, *ACS Appl. Nano Mater.*, 2020, **3**, 8997–9008.
44 Y. Liu, A. J. Howarth, N. A. Vermeulen, S.-Y. Moon, J. T. Hupp and O. K. Farha, *Coord. Chem. Rev.*, 2017, **346**, 101–111.
45 G. W. Peterson, M. R. Destefano, S. J. Garibay, A. Ploskonka, M. McEntee, M. Hall, C. J. Karwacki, J. T. Hupp and O. K. Farha, *Chem. – Eur. J.*, 2017, **23**, 15913–15916.
46 S. Pareek and J. K. Quamara, *J. Mater. Sci.*, 2018, **53**, 604–612.
47 R. Zhang, B. Du, Q. Li, Z. Cao, G. Feng and X. Wang, *Appl. Surf. Sci.*, 2019, **466**, 956–963.
48 M. B. Nguyen, G. H. Le, T. D. Nguyen, Q. K. Nguyen, T. T. Pham, T. Lee and T. A. Vu, *J. Hazard. Mater.*, 2021, **420**, 126560.
49 A. S. Eltaweil, E. M. A. El-Monaem, G. M. El-Subruiti, M. M. A. El-Latif and A. M. Omer, *RSC Adv.*, 2020, **10**, 19008–19019.
50 B. Ng, L. K. Putri, X. Y. Kong, Y. W. Teh, P. Pasbakhsh and S. Chai, *Adv. Sci.*, 2020, **7**, 1903171.
51 M. Taddei, G. M. Schukraft, M. E. A. Warwick, D. Tiana, M. J. McPherson, D. R. Jones and C. Petit, *J. Mater. Chem. A*, 2019, **7**, 23781–23786.
52 M. B. Nguyen, X. N. Pham and H. V. Doan, *RSC Adv.*, 2021, **11**, 31738–31745.